Journal of Materials Science: Materials in Electronics (2018) 29:20329–20338
https://doi.org/10.1007/s10854-018-0167-x

An approach for photodegradation mechanism at $TiO_2/SrTiO_3$ interface

Ubirajara Coleto Jr.[1,2] · Rafael A. C. Amoresi[1,3] · Vinícius Teodoro[4] · Isabela M. Iani[1] · Elson Longo[4] · Maria A. Zaghete[1] · Leinig A. Perazolli[1]

Received: 20 June 2018 / Accepted: 4 October 2018 / Published online: 6 October 2018

Abstract
$TiO_2/SrTiO_3$ heterojunction powders were obtained and characterized, and their photocatalytic potential was evaluated. The formation of the solid–solid interface was evidenced by secondary-phase formation in the interface region, which was observed using transmission electron microscopy. The photocatalytic efficiency of the $TiO_2/SrTiO_3$ heterojunction was higher than that of pure TiO_2 and $SrTiO_3$ samples. The photocatalytic behavior was investigated via scavenger experiments, which indicated that the mechanism of charge transfer for the heterojunction was the direct transfer of the electrons at the interface. A surface compositional analysis of the materials revealed that effective electronic-transfer properties of the materials are more important than the content of pre-adsorbed species on the surface for redox reactions. Photoluminescence spectroscopy analyses showed a reduction in the photoluminescent intensity for the heterojunction and emission in distinct regions depending on the defects formed in the heterojunction. These differences in behavior may be related to the different photocatalytic responses observed for pure compounds and heterojunctions; a broad analysis indicates that the mono ($V_O^{\cdot}$) and double ($V_O^{\cdot\cdot}$) ionized vacancies affect the performance of the photocatalyst in the degradation of micropollutants.

1 Introduction

New models of oxide materials for applications to multiple devices [1, 2], have been constructed using nanometric heterojunctions [3, 4]. The $TiO_2/SrTiO_3$ heterojunction is one of these. Titanium dioxide (TiO_2) is an *n*-type semiconductor with a bandgap energy of approximately 3.2 eV. It has high photocatalytic activity and is inexpensive and non-toxic [5]. This material in the anatase crystalline phase has been studied for photocatalysis owing to the low recombination rate of electrons and holes, that is, charge carriers. Upon being excited on TiO_2, these charge carriers can follow different paths, migrating to the surface of the particle and reacting with donor and acceptor molecules of electrons or recombining at both bulk and surface trapping sites. Since the recombination and charge-carrier transfer processes follow distinct timescales, varying from femtoseconds to microseconds, thus the increases in recombination time allows an increase in charge-carrier transfer rate, for the molecules to be degraded [6]. Another important feature of TiO_2 photoactivityis its hydrophilicity [7]. This is mainly due to the defect states of Ti^{4+}/Ti^{3+} in the crystal lattice [6], which facilitate the generation of radical species. In addition to the intrinsic electronic characteristics of the binary oxide structure, the predominance of surface facets (zero- to three-dimensional structures) that are exposed to the reaction medium [8], and the use of dopants in the crystalline structure [9] influence the photoactivity of the material by retarding the charge-carrier recombination.

The $SrTiO_3$ (STO) used as the junction in this work is a perovskite-type oxide, in which Sr^{2+} occupies the vertices surrounding the octahedral [TiO_6] cluster at the center of a cubic crystalline system [10]. STO is typically an *n*-type semiconductor with a bandgap energy of approximately 3.2 eV [11]; however, its electronic band potentials differ from those of TiO_2, which allows a shift of the absorption of light energy and hence the modulation of the optical

✉ Rafael A. C. Amoresi
rafaelciola@yahoo.com.br

1 LIEC-Chemistry Institute, São Paulo State University-UNESP, Araraquara, SP, Brazil

2 Department of Chemistry, Federal Institute of São Paulo-IFSP, Catanduva, SP, Brazil

3 Faculty of Engineering of Guaratingueta-UNESP, São Paulo, SP, Brazil

4 LIEC-Department of Chemistry, Universidade Federal de São Carlos-UFSCAR, São Carlos, SP, Brazil

properties of heterojunction materials [12]. For this perovskite, the valence band (VB) is predominantly composed of O 2p orbitals, with a minor contribution of Ti 3d orbitals, whereas the conduction band (CB) is mainly composed of Ti 3d orbitals and Sr 3d orbitals at higher energies [13–15]. Luo et al. [16] evaluated the surface termination at Ti and Sr sites for the $SrTiO_3$ structure and related them to the photocatalytic activity for CO_2 reduction. They observed surface structural distortions and high activity for photoreduction at the Ti surface termination. Kato and Kudo [17] observed that electronic transitions between holes in the VB and dopant ions, which have photoluminescent behavior, occur more easily in the chemical environment of the VB of $SrTiO_3$ than in TiO_2. This suggests that the chemical environment around the Ti^{4+} ions is propitious to the photoactivity and that the perovskite STO promotes the electronic transitions [8, 9, 16, 17].

In this sense, heterojunctions formed between $SrTiO_3$ and TiO_2 obtained via different processes and their photocatalytic responses have been analyzed. The higher photocatalytic efficiency of the heterojunction compared with pure materials is mainly attributed to the efficient separation of photogenerated charge carriers at the interface [18–20]. Ng et al. [18] evaluated the growth of $SrTiO_3$ nanocubes on TiO_2 anatase nanowires, in which the $SrTiO_3$ with a cube-like morphology contains predominantly Sr on the surface, leading to a p-type semiconductor, which captures the photoelectrons generated in the heterojunction. Wang et al. [21] prepared heterojunctions by growing colloidal TiO_2 above $SrTiO_3$ and showed that both the semiconductors obtained via this process were n-type. The higher photocatalytic activity was due to the isolation of the charge carriers on opposite directions of the heterojunction. Zhang et al. [20] obtained $SrTiO_3/TiO_2$ heterojunctions via electrochemical anodization that showed high photoelectrochemical performance up to a certain $SrTiO_3$ growth limit on the TiO_2 nanotube. They discussed this behavior in relation to the growth and dispersion of perovskite nanocrystallites on the binary oxide. Therefore, studies on heterojunctions are directly related to the processing to which they are submitted, the coupling order of the phases, the growth morphology, and the mechanism of charge transfer in the heterojunction.

For the simplest photocatalytic mechanism of binary oxide (TiO_2) semiconductors, the photoexcited electrons (e^-) in the CB and the holes (h^+) in the VB dominate the beginning of the photocatalytic mechanism [22, 23], e.g., for the degradation of several organic pollutants [5], or the production of biofuels [24]. However, despite the wide field of applications, there is a gap related to the mechanism of charge carriers in heterojunction materials. In this study, we evaluated the photocatalytic activity of $TiO_2/SrTiO_3$ heterojunctions for Rhodamine B (RhB) dye degradation. The charge-carrier transfer mechanisms were evaluated for both the pure materials and the heterojunction materials. Finally, the electronic behavior of the materials was elucidated via spectroscopic analyses of the photoelectrons excited by X-rays and photoluminescence (PL).

2 Materials and methods

The preparation of the materials was described in detail by Amoresi et al. [12]. According to this method, we prepared a Ti sol–gel solution with titanium isopropoxide (Sigma-Aldrich, 97%), acetic acid (Qhemis, 99.7%), and isopropyl alcohol (Vetec, 99.5%), at a molar ratio of 1:4:0.7. Separately, we prepared an electrosterically stabilized suspension of $SrTiO_3$ particles previously obtained by Pechini method [25], using acrylic acid, 2-methoxyethanol (Sigma-Aldrich, 99%), isopropyl alcohol (Vetec, 99.5%), and polyvinyl alcohol (Vetec, 99%). This electrosterically stabilized suspension of $SrTiO_3$ particles was added to a Ti sol–gel solution to obtain heterojunctions with 1 and 5 wt% of $SrTiO_3$ related to TiO_2, and then the mixture was kept at 25 °C under stirring for 24 h for gel formation. Subsequently, the gel was dried at 100 °C for 24 h in an oven, followed by heat treatment at 500 °C for 4 h.

The materials were characterized via X-ray diffraction (XRD) using a Rigaku-Rint 2000, field-emission scanning electron microscopy (FE-SEM) using a JEOL model 7500F, and transmission electron microscopy (TEM) using an FEI/PHILIPS CM120. PL spectra were collected using a Thermo Jarrell Ash 27-cm monochromator with a Hamamatsu photomultiplier (model R955). A krypton laser (Coherent Innova 200) with a wavelength output at 350 nm was used as the excitation source. X-ray photoelectron spectroscopy (XPS) measurements were performed using a Scienta Omicron ESCA, with an Al Kα X-ray source. Photocatalytic experiments were performed in a reactor (lamp $\lambda_{max} = 254$ nm, 11W, Osram, Puritec HNS 2G7), with air bubbling and constant stirring. Here, 70 mg of photocatalyst (0.1 g L^{-1}) was added to 700 mL of an RhB dye solution (10^{-5} M), and the suspension was kept in an ultrasonic bath for 20 min to quickly reach the adsorption/desorption equilibrium. Photocatalytic experiments using scavengers as markers to predict the degradation mechanism were conducted. The reagents used were 2Na-EDTA, p-benzoquinone, and isopropanol. All the scavengers were added to the suspension before the ultrasonication. Aliquots were withdrawn at certain times, centrifuged, and analyzed via absorption spectroscopy using a spectrophotometer (Femto Cirrus 80PR) at 554 nm.

3 Results and discussion

The XRD patterns for the samples obtained in this study are presented in Fig. 1. The TiO_2 powders show only a polycrystalline anatase phase, with the space group I41/

amd (ICSD no. 9852). The $SrTiO_3$ powders exhibit a pure cubic phase, with the space group Pm-3m (ICSD no. 23076). The heterojunction TiO_2/1%$SrTiO_3$ shows only the anatase phase, which is related to TiO_2. For this sample, only TiO_2 peaks are observed, owing to the small amount of the $SrTiO_3$ phase compared with TiO_2. On the other hand, for the TiO_2/5%$SrTiO_3$ heterojunction, in addition to the anatase-phase peaks of TiO_2, peaks related to the $SrTiO_3$ cubic phase were observed. For both heterojunctions, peaks were observed with a full width at half maximum greater than that of the pure materials. This is attributed to the smaller crystallite size of the samples with the insertion of the $SrTiO_3$ phase during the synthesis [26]. Figure 2 shows FE-SEM and TEM images of the samples. Figure 2a shows FE-SEM images of TiO_2, indicating spherical particles with an average particle size of 10 nm. Figure 2b shows FE-SEM images of the $SrTiO_3$ powders, in which a spherical shape ranging in size from 50 to 100 nm is observed. The preparation route for the TiO_2/$SrTiO_3$ heterojunctions resulted in particles with a smaller average size compared with the pure materials, with values ranging from 7.7 to 10.5 nm, as shown in the TEM images of Fig. 2c, d.

Figure 3 shows the EDX mapping of both heterojunction samples. In both heterojunctions, Ti ions are fully distributed throughout the samples. This is a common element between the two materials, acting as a matrix ion in TiO_2 and a lattice former in $SrTiO_3$. Oxygen showed more intense regions of predominance owing to the surface roughness of the sample. The Sr ions, which indicate the different concentrations of the $SrTiO_3$ phase, showed lower predominance in the sample with 1% $SrTiO_3$ than in the sample with 5% $SrTiO_3$, as expected. Therefore, the EDX mapping corroborates the proportional formation of the heterojunction and the homogeneity of the chemical composition everywhere on the particle in both heterojunction samples.

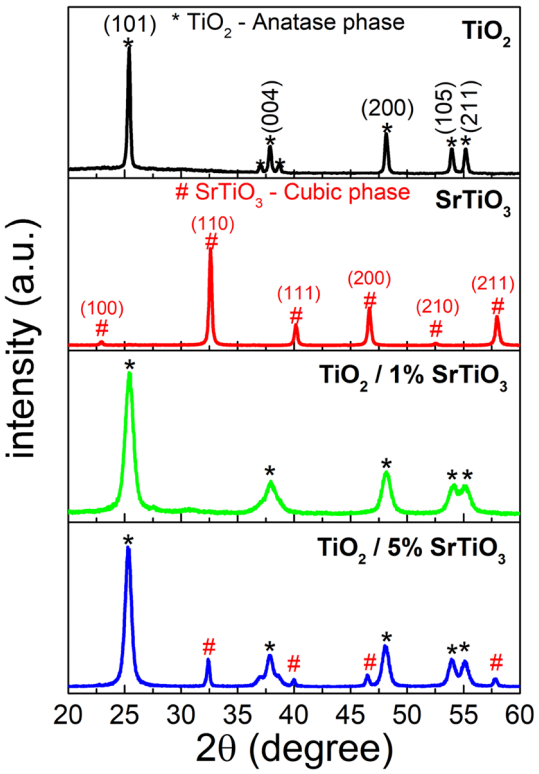

Fig. 1 XRD patterns for the TiO_2 and $SrTiO_3$ samples and the heterojunctions obtained with 1% and 5% of $SrTiO_3$

The formation of a solid–solid interface between TiO_2 and $SrTiO_3$ was evidenced by high-resolution TEM (HRTEM), as shown in Fig. 4a. The HRTEM image reveals an interface region in which TiO_2 grows on the crystalline surface of $SrTiO_3$ particles, as shown in Fig. 4b. This is confirmed by the corresponding crystal lattice planes for both $SrTiO_3$ and TiO_2. To facilitate interpretation, the image was divided into regions. In Fig. 4a, region 1 indicates the interplanar distance of the crystal lattice (2.26 Å), according to the (111) plane of the cubic $SrTiO_3$. In region 2, next to the plans of $SrTiO_3$, an interface region was verified. In this region, the calculated interplanar distance was 2.10 Å, which does not correspond to any of the anatase phases of TiO_2 or to any plane of the cubic phase of $SrTiO_3$. Possibly, this interplanar distance corresponds to the (− 303) plane of the monoclinic phase of TiO_2 (ICSD no. 65-6429). Region 3 shows the predominance of the (101) planes of the TiO_2 anatase phase, with an interplanar distance of 3.52 Å.

The aforementioned results indicate that the TiO_2/$SrTiO_3$ heterojunction interface is composed of intermediary phases of the predominant TiO_2 structure. The direct growth of the (101) plane of the anatase phase of TiO_2 on the surface of the (111) plane of the cubic phase of $SrTiO_3$ would be unstable. This interface would generate a stress of 56% owing to the difference between the interplanar distances of 3.52 Å and 2.26 Å. However, considering the plane of the monoclinic phase in TiO_2 with an interplanar distance of 2.10 Å, the generated interface stress decreases to 7% on the (111) surface of $SrTiO_3$. The growth of TiO_2 was not observed on any surface besides the (111) plane of $SrTiO_3$. Some studies demonstrated the growth of crystalline structures only at interfaces with close interplanar distances [27, 28] or atomic planes that fit within each other [29, 30]. Figure 4b shows a magnification of a part of Fig. 4a, with a dashed-line rectangle, indicating the crystalline growth of the interface region. This suggests that there is a secondary phase in the medium range that forms the interface in relation to the TiO_2 main phase. This type of interface generates different defect levels in heterojunctions and influences the electronic properties, as indicated by the following photocatalytic results.

Figure 5a shows the photocatalytic activity of all the samples for photodegradation of the RhB solution. Photolysis analysis, i.e., the degradation experiment of the RhB solution without a photocatalyst, was also performed, showing the degradation

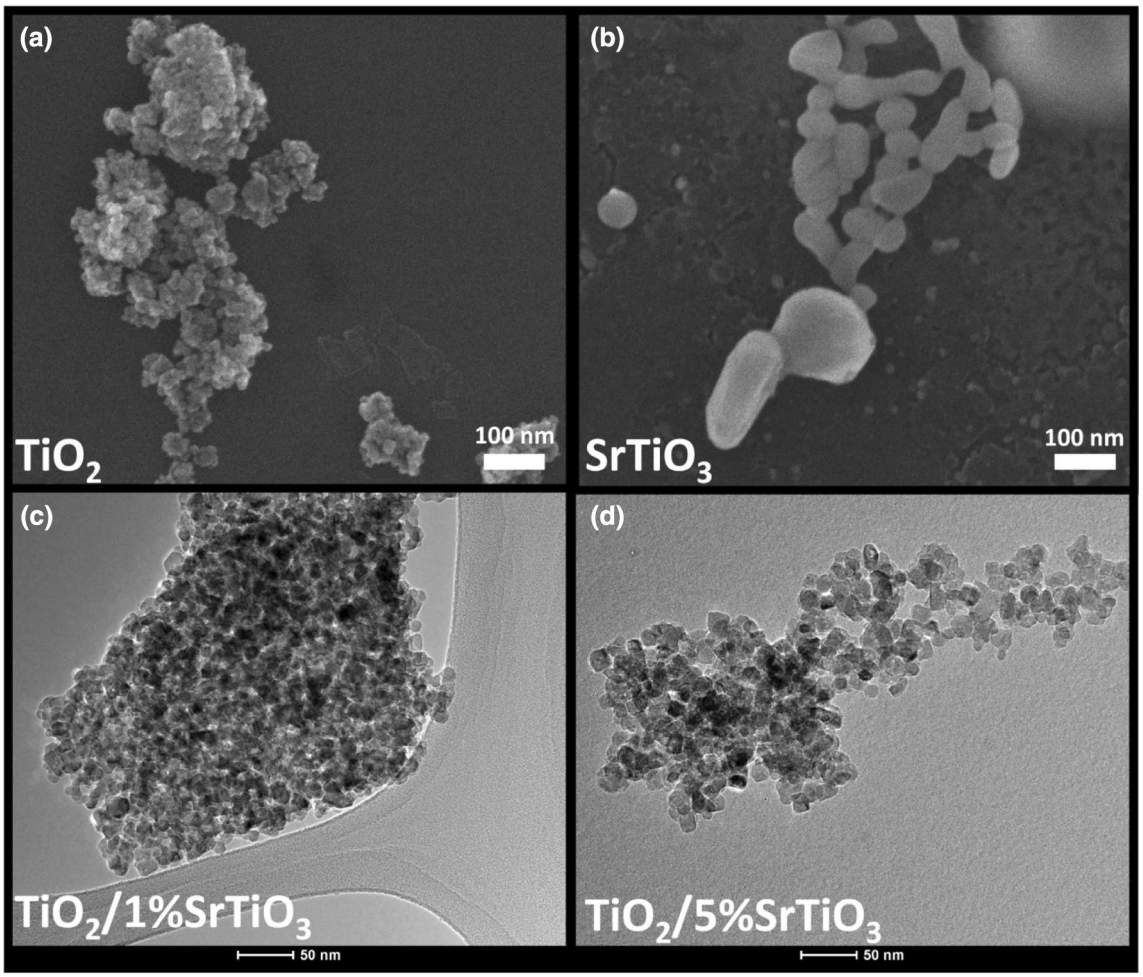

Fig. 2 FE-SEM images of the **a** TiO_2 and **b** $SrTiO_3$ samples; TEM images of the **c** TiO_2/1%$SrTiO_3$ and **d** TiO_2/5%$SrTiO_3$ heterojunctions

results only from the light used in the experiment. Photocatalytic experiments were performed using hole, hydroxyl radicals, and superoxide radical scavengers to analyze the photocatalytic mechanisms of the materials. The analyzed samples were TiO_2/1%$SrTiO_3$, considering that this material showed the highest photocatalytic activity, and pure $SrTiO_3$ and TiO_2, for comparison. The photocatalytic results for all samples are shown in Table 1, including the rate constant, photodegradation percentage after 120 min of reaction, and the calculated and observed half-life times. In a general mode, the heterogeneous photocatalysis process using low-solubility semiconductors as a photocatalystis considered a pseudo-first order reaction owing to the low initial concentration of organic compounds and the constant concentration of the photocatalyst [31–33]. Thus, to verify the reaction order and determine the rate constant, the Langmuir–Hinshelwood model, which is described by Eq. (1), was applied to all samples.

$$\ln\frac{A_0}{A_t} = k\mathrm{t} \tag{1}$$

Here, A_0 and A_t are the initial concentration and the concentration at a given time, respectively; k is the rate constant; and t is the reaction time. If the reaction is pseudo-first-order, the plot of $\ln(A_0/A_t)$ versus time results in a sequence of points that can be approximately fitted in a straight line, where the angular coefficient is the k value. The half-life time of pseudo-first-order reactions can be calculated using Eq. (2). According to the plot results (Fig. 5b), all the photocatalytic processes of the obtained samples were well-fitted as pseudo-first-order reactions.

$$t_{1/2} = \frac{\ln 2}{k} \tag{2}$$

The photocatalytic performance has a logical relationship with the rate constant; as can be observed, the TiO_2/1%$SrTiO_3$ sample exhibits a higher rate constant for the photodegradation of the RhB solution. The lowest half-life time 46.5 min calculated and 49.6 min observed—was also obtained for this material. The enhancement of the photocatalytic activity of the heterojunctions compared with

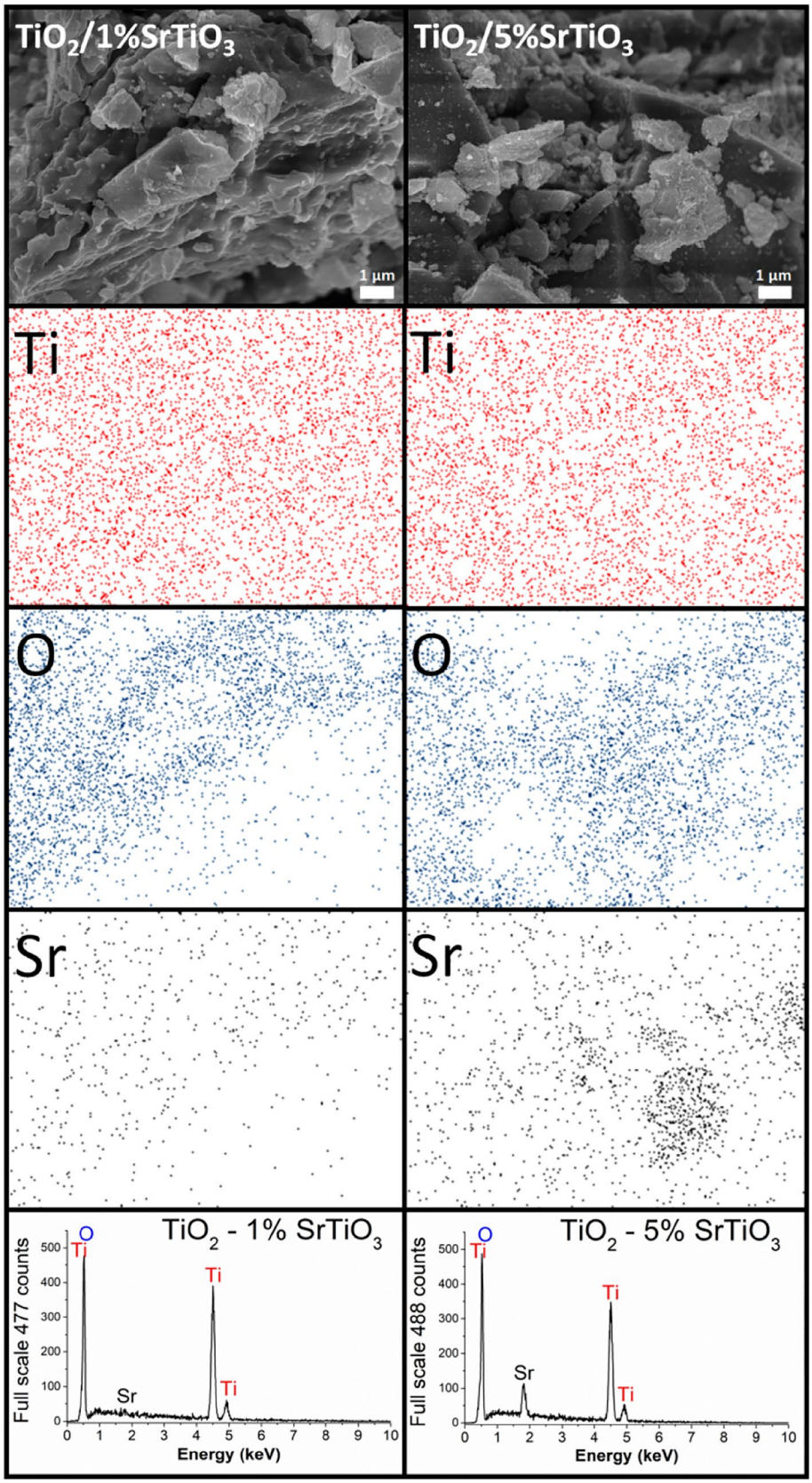

Fig. 3 EDX mapping of the heterojunctions. From top to bottom, the figure shows the FE-SEM analyses; the mapping for the Ti, O, and Sr ions; and the energy versus species count graph. The left and right sides correspond to the TiO_2/1%$SrTiO_3$ and TiO_2/5%$SrTiO_3$ heterojunctions, respectively

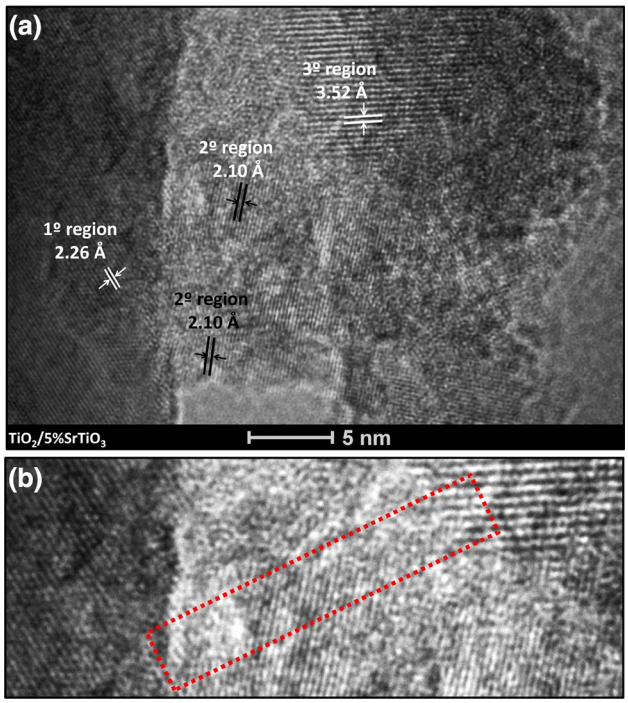

Fig. 4 **a** HRTEM images of the TiO_2/5%$SrTiO_3$ heterojunction interface region; **b** magnification of the center of the figure, showing the crystalline growth of the heterostructure

pure TiO_2 is mainly related to the charge-carrier transfer in the interface region [6]. Figure 5c shows the photodegradation of the RhB solution as a function of time, where scavengers were used as the control for the pure $SrTiO_3$ sample. The isopropyl alcohol, p-benzoquinone, and 2Na-EDTA act as scavengers for hydroxyl radicals (HO·), superoxide radicals ($O_2^{\cdot-}$), and holes (h^+), respectively. The experiments for $SrTiO_3$ show that there was higher photocatalytic activity after the addition of the scavengers. Such behavior was expected for $SrTiO_3$ because this structure exhibits high electron–hole recombination [34]. Adding the scavengers, prevents the recombination of the charge carriers and increases the photocatalytic activity of the $SrTiO_3$ [35, 36]. For the TiO_2 sample, as shown in Fig. 5d, the experiment using hole scavengers indicated their major contribution to the photodegradation mechanism, as their absence led to lower RhB photodegradation (34% after 120 min of reaction). It was also observed that until 30 min of reaction, the superoxide radicals had no significant effect on the photodegradation mechanism of pure TiO_2, as their absence did not affect the photodegradation efficiency in this time. Figure 5e shows the photocatalytic reaction scheme for pure TiO_2. Figure 5f shows the photodegradation of the RhB solution using scavengers as control for the TiO_2/1%$SrTiO_3$ sample. As can be seen, the holes have a major contribution to the photodegradation for the heterojunction samples; however, the superoxide radicals also contribute significantly, being almost the same degree. The photodegradation behavior of the TiO_2/1%$SrTiO_3$ sample agrees well with the charge transfer mechanism for heterojunctions in solid-state physics, as holes and electrons migrate in opposite directions [37].

The photoexcited electrons in the CB of $SrTiO_3$ migrate to the CB of TiO_2 owing to its higher reduction potential compared with $SrTiO_3$, as indicated in Fig. 5g. The dashed lines between both CBs represent the band bending resulting from the band alignment of these bands due to their different reduction potentials, indicating the formation of a solid–solid interface. The similar degrees of contribution between the superoxide radicals and holes for the TiO_2/1%$SrTiO_3$ sample confirm the effective charge transfer at the TiO_2/$SrTiO_3$ interface, which increase the recombination time. They also confirm the particle-size homogeneity throughout the sample, once both holes and electrons reach the surface particles of the materials and react with species at similar rates. A slight difference between the contributions of the holes and superoxide radicals is possible owing to the direct and indirect reactions; i.e., holes directly oxidize species adsorbed on the surface particles, while electrons first reduce the adsorbed O, which then reacts with species, resulting in a slight decrease in the rate for this photodegradation route. Additionally, the greater contribution of the holes possibly arises from the generation of hydroxyl radicals [38, 39] and the predominance of TiO_2 compared with $SrTiO_3$ in the sample.

The surface chemical environments of the samples were investigated using XPS, and Fig. 6a shows the survey spectra. The elements Ti and O are present in the regions of 458 and 530 eV, respectively, and the Sr peak appears at 133 eV, which is clearly observed by high-resolution measurement of peaks (inset). According to the results for all the samples, the Ti 2p peaks indicate + 4 oxidation states (Fig. 6b, d, f). Despite both samples having the same oxidation state of ions, a slight difference in the peak shapes for O 1s is observed. The peaks were deconvoluted to obtain additional information (Fig. 6c, e, g). These results indicate O bound to C, e.g., carbonate, carbon dioxide (~ 533 eV), hydroxide, and surface defects (~ 531 eV), as well as O bound to the lattice (~ 530 eV). However, interestingly, the O peaks showed a difference in the O content from the hydroxide in the samples. For pure TiO_2, a higher content of hydroxide O was observed compared with the TiO_2/1%$SrTiO_3$ and TiO_2/5%$SrTiO_3$ samples, indicating a higher content of hydroxyl ions adsorbed on the TiO_2 surface. It is known for single-phase materials that hydroxyl sites are favorable for photocatalytic activity [40, 41]. Nonetheless, the photocatalytic performance of the heterojunction samples was higher than that of pure TiO_2, even with a lower content of hydroxyl ions adsorbed on the heterojunction surface. This observation confirms the effectiveness and importance of the electronic-transfer properties of materials, as the charge

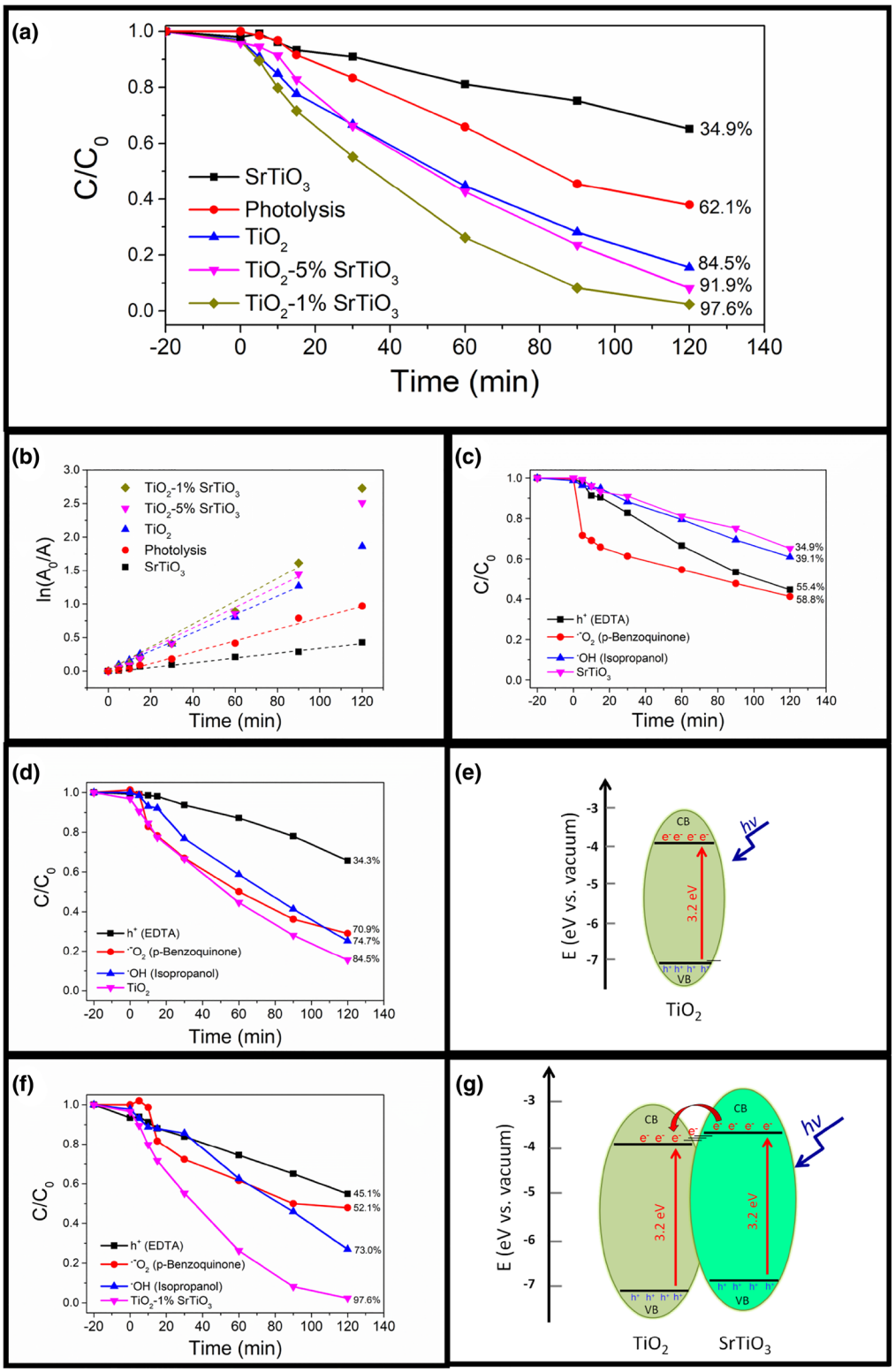

Fig. 5 **a** Photocatalytic activity for photocatalysts and photolysis in the degradation of RhB; **b** $\ln(A_0/A_t)$ versus time for degradation; the photocatalytic activity using scavengers for the **c** $SrTiO_3$, **d** TiO_2, and **f** TiO_2/1%$SrTiO_3$ samples. Schematic of the photocatalytic mechanism for the **e** TiO_2 and **g** TiO_2/1%$SrTiO_3$ samples

Table 1 Photocatalytic data for the samples and photolysis for the discoloration of the Rh-B dye solution

Sample	Discoloration (120 min) (%)	$k_{app} \times 10^{-2}$ (min^{-1})	$t_{1/2}$ (calculated) (min)	$t_{1/2}$ (observed) (min)
$SrTiO_3$	34.9	0.34	203.9	–
Photolysis	62.1	0.85	81.5	83.3
TiO_2	84.5	1.36	51.0	52.9
TiO_2–5%$SrTiO_3$	91.9	1.60	43.3	50.6
TiO_2–1%$SrTiO_3$	97.6	1.75	39.6	35.3

carriers are responsible for the redox reactions of adsorbed species.

However, the heterojunction with 1% of $SrTiO_3$ exhibits greater photocatalytic activity than that with 5% of $SrTiO_3$. To investigate the behavior of the photogenerated electron–hole pairs, the PL spectra for TiO_2 and the heterojunctions were obtained in the range of 350–850 nm, and the results are plotted in Fig. 7. The spectra for the pure materials indicate that the TiO_2 has an emission center at 550 nm—in the green wavelength region—with the highest PL intensity among the materials. The pure $SrTiO_3$ exhibits photoluminescent emission centered at 445 nm—the blue region—with low photoluminescent intensity. The heterojunction with 1% of $SrTiO_3$ exhibits a major emission contribution in the blue region, and that with 5% exhibits broad emission bands throughout the spectrum. Both heterojunctions exhibit PL intensities lower than that of pure TiO_2. This reduction in the PL intensity suggests that the recombination of electron–hole pairs was reduced compared with that for pure TiO_2, owing to the formation of the heterojunction, which resulted in charge transfer at the interface. However, regarding the TiO_2/1%$SrTiO_3$ and TiO_2/5% $SrTiO_3$ heterojunctions, the TiO_2/1%$SrTiO_3$ heterojunction shows higher emission in the region equivalent to the higher energy. The TiO_2/5%$SrTiO_3$ heterojunction shows a shift of the emission band related to that of TiO_2/1%$SrTiO_3$, emitting in region of lower energy. The difference resulting from these two types of emission behavior has been discussed in detail by our group [12, 42]. In the case of the heterojunction with 1% of $SrTiO_3$, the formation of clusters with O vacancies of the monoionized type ($[TiO_5 \cdot V_O^{\cdot}]$), which are highly energetic and have emission in the blue region, was favored [42, 43]. The chemical behavior for this type of heterojunction is indicated by Eqs. (3) and (4) for the TiO_2 and $SrTiO_3$ regions of the heterojunction, respectively.

$$[TiO_6]_o^x + [TiO_5 \cdot V_o^x]_d \rightarrow [TiO_6]_o^{'} + [TiO_5 \cdot V_o^{\cdot}]_d \quad (3)$$

$$[SrO_{12}]_o^x + [SrO_{11} \cdot V_o^x]_d \rightarrow [SrO_{12}]_o^{'} + [SrO_{11} \cdot V_o^{\cdot}]_d \quad (4)$$

The subscript *o* indicates the ordered cluster, and the subscript *d* indicates the disordered cluster. V_o^x and $V_o^{\cdot}$ indicate

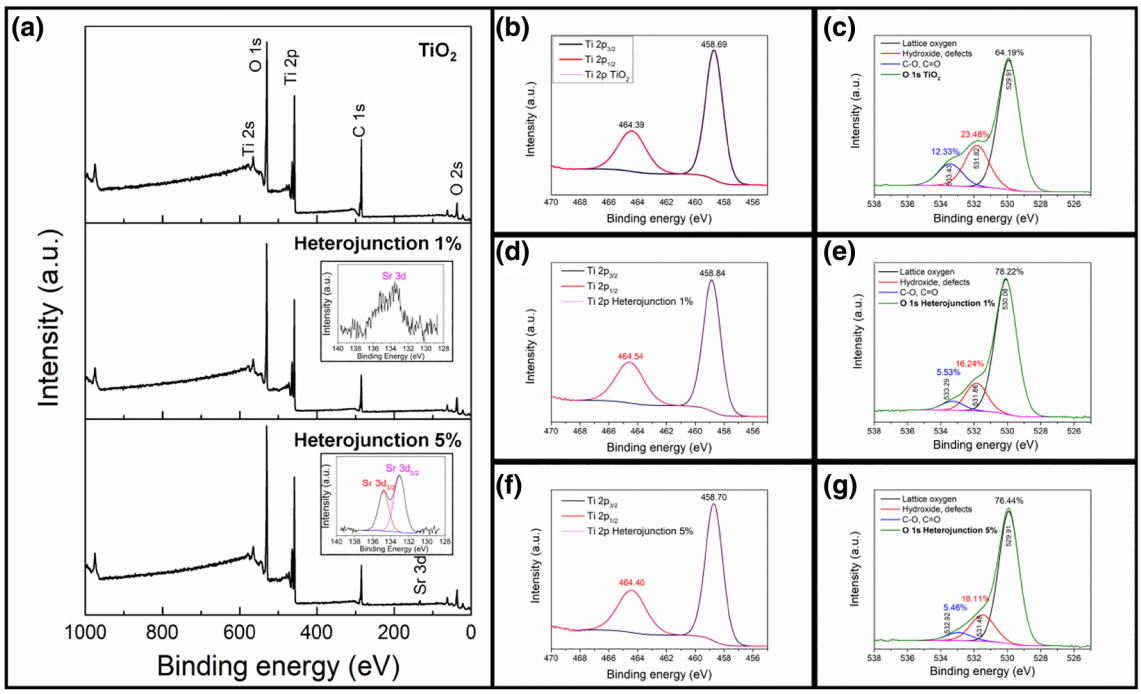

Fig. 6 XPS spectra. **a** Survey spectra, where the inset shows the high-resolution spectra for the Sr 3d species; (**b, d, f**) spectra for the Ti 2p species and (**c, e, g**) for the O 1s species of the TiO_2, TiO_2/1%$SrTiO_3$, and TiO_2/5%$SrTiO_3$ samples, respectively

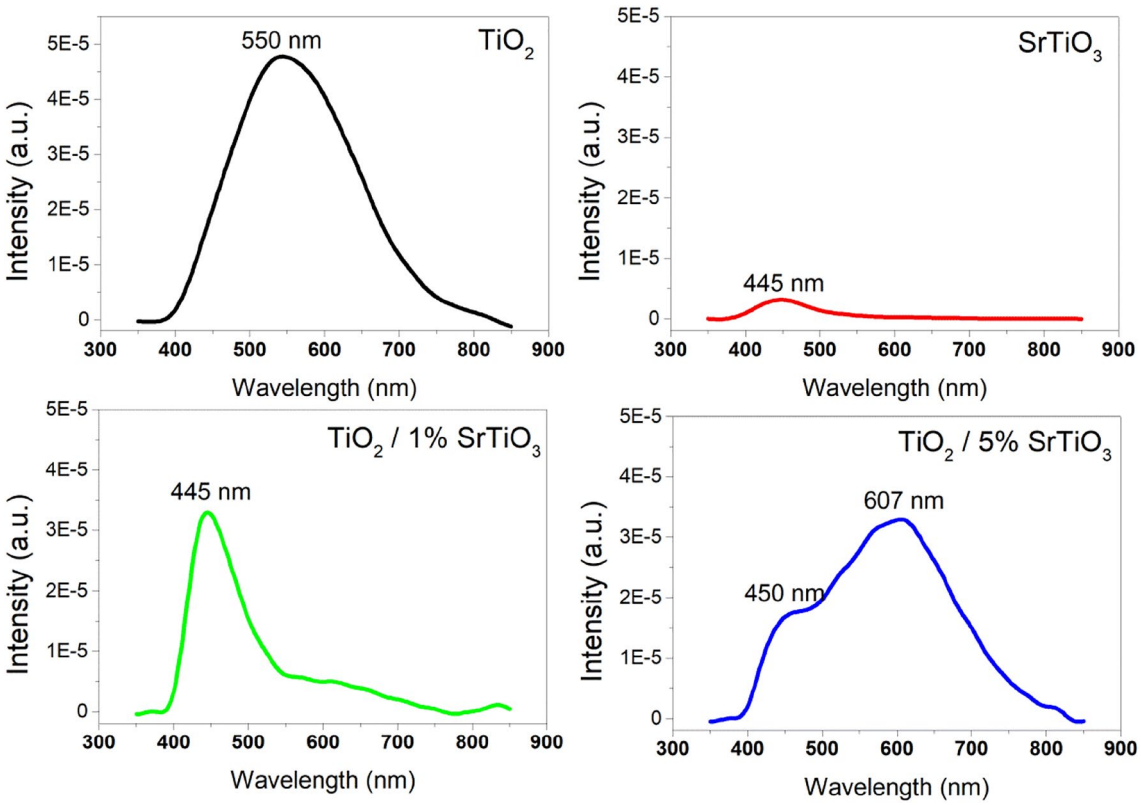

Fig. 7 PL spectra obtained under 350 nm excitation for pure TiO_2 and $SrTiO_3$ samples and heterojunctions with 1% and 5% $SrTiO_3$

neutral and monoionized O vacancies, respectively, and the superscript $'$ indicates an electron, according to the Kröger–Vink notation. For the heterojunction with 5% of $SrTiO_3$, doubly ionized vacancies, $V_O^{\cdot\cdot}$, are formed, as indicated by Eqs. (5)–(8):

$$[TiO_6]_o^x + [TiO_5 \cdot V_o^x]_d \rightarrow [TiO_6]_o^{'} + [TiO_5 \cdot V_o^{\cdot}]_d \quad (5)$$

$$[TiO_5 \cdot V_o^{\cdot}]_d + [TiO_6]_o^x \rightarrow [TiO_5 V_o^{\cdot\cdot}]_d + [TiO_6]_o^{'} \quad (6)$$

$$[SrO_{12}]_o^x + [SrO_{11} \cdot V_o^x]_d \rightarrow + [SrO_{11} \cdot]_d \quad (7)$$

$$[SrO_{12}]_o^x + [SrO_{11} \cdot V_o^{\cdot}]_d \rightarrow [SrO_{12}]_o^{'} + [SrO_{11} V_o^{\cdot\cdot}]_d \quad (8)$$

Considering that the heterojunction with 1% of $SrTiO_3$ exhibited the predominance of defects of monoionized O vacancies and considering the higher photocatalytic activity for this sample, it was inferred that this type of defect increased the recombination time of the charge carriers compared with the doubly ionized vacancies, $V_o^{\cdot\cdot}$, thus favoring the photocatalytic process. The significant participation of monoionized O vacancies in the photodegradation reactions can be expected, as this type of defect can act as donor and acceptor of electrons, generating doubly ionized and neutral O vacancies, respectively, rather than doubly ionized vacancies that can accept electrons only. Thus, the monoionized O vacancy is considered as an electronic bridge for the charge-carrier transfer.

4 Conclusions

$TiO_2/SrTiO_3$ heterojunctions showed higher photocatalytic efficiency, which contributed to their better photodegradation performance, than pure TiO_2 and $SrTiO_3$ samples. The main contributions to the photodegradation mechanism of the heterojunctions, which was experimentally observed, were from electrons and holes, confirming the effective charge transfer at the solid–solid interface. In addition, XPS analyses indicated that the photogenerated charge transfer in the photocatalysts is more important than the content of pre-adsorbed species on the particle surface for the photodegradation of organic dyes. PL analyses revealed that defects—particularly monoionized O vacancies—in the $TiO_2/SrTiO_3$ heterostructure favored the photocatalytic activity. This confirms that understanding the electronic properties of materials is fundamental for scientific knowledge and modeling desirable properties.

Acknowledgements This work was supported by the São Paulo Research Foundation (Grant CEPID/CDMF-FAPESP, process no. 2013/07296-2, and 2017/19143-7) and the National Council for Scientific and Technological Development (CNPq). We are also grateful to the LMA-IQ for providing the FEG-SEM facilities.

References

1. S. Bai, W. Guo, J. Sun, J. Li, Y. Tian, A. Chen, R. Luo, D. Li, Sens. Actuators B. Chem. **226**, 96–103 (2016)
2. P.P. Ortega, L.S.R. Rocha, C.C. Silva, M. Cilense, R.A.C. Amoresi, E. Longo, A.Z. Simões, Ceram. Int. **42**, 16521–16528 (2016)
3. A. Ohtomo, H.Y. Hwang, Nature. **427**, 423–426 (2004)
4. D.E. Motaung, G.H. Mhlongo, P.R. Makgwane, B.P. Dhonge, F.R. Cummings, H.C. Swart, S.S. Ray, Sens. Actuators B. Chem. **254**, 984–995 (2018)
5. C.B.D. Marien, T. Cottineau, D. Robert, P. Drogui, Appl. Catal. B Environ. **194**, 1–6 (2016)
6. A. Fujishima, X. Zhang, D.A. Tryk, Surf. Sci. Rep. **63**, 515–582 (2008)
7. K. Hashimoto, H. Irie, A. Fujishima, Jpn. J. Appl. Phys. **44**, 8269–8285 (2005)
8. K. Nakata, A. Fujishima, J. Photochem. Photobiol. C Photochem. Rev. **13**, 169–189 (2012)
9. J. Schneider, M. Matsuoka, M. Takeuchi, J. Zhang, Y. Horiuchi, M. Anpo, D.W. Bahnemann, Chem. Rev. **114**, 9919–9986 (2014)
10. S. Zeng, P. Kar, U.K. Thakur, K. Shankar, Nanotechnology. **29**, 52001 (2018)
11. W. Zhao, N. Liu, H. Wang, L. Mao, Ceram. Int. **43**, 4807–4813 (2017)
12. R.A.C. Amoresi, V. Teodoro, G.F. Teixeira, M.S. Li, A.Z. Simões, L.A. Perazolli, E. Longo, M.A. Zaghete, J. Eur. Ceram. Soc. **38**, 1621–1631 (2018)
13. H.-C. Chen, C.-W. Huang, J.C.S. Wu, S.-T. Lin, J. Phys. Chem. C **116**, 7897–7903 (2012)
14. K. Van Benthem, C. Elsässer, R.H. French, J. Appl. Phys. **90**, 6156–6164 (2001)
15. E. Drożdż, A. Koleżyński, RSC Adv. **7**, 28898–28908 (2017)
16. C. Luo, J. Zhao, Y. Li, W. Zhao, Y. Zeng, C. Wang, Appl. Surf. Sci. **447**, 627–635 (2018)
17. H. Kato, A. Kudo, J. Phys. Chem. B. **106**, 5029–5034 (2002)
18. J. Ng, S. Xu, X. Zhang, H.Y. Yang, D.D. Sun, Adv. Funct. Mater. **20**, 4287–4294 (2010)
19. A. Fujischima, X. Zhang, D.A. Tryk, Surf. Sci. Rep. **63**, 515–582 (2008)
20. J. Zhang, J.H. Bang, C. Tang, P.V. Kamat, ACS Nano **4**, 387–395 (2010)
21. L. Wang, Z. Wang, D. Wang, X. Shi, H. Song, X. Gao, Solid State Sci. **31**, 85–90 (2014)
22. J. Haider, A. Anbari, O. Le Corre, P. Ferrão, Energy Procedia **119**, 332–345 (2017)
23. R.L. Ziolli, W.F. Jardim, Quim. Nova **21**, 319–325 (1998)
24. G. Corro, U. Pal, N. Tellez, Appl. Catal. B Environ. **129**, 39–47 (2013)
25. G. Gasparotto, G.F. Teixeira, M.A. Cebim, J.A. Varela, L.A. Perazolli, M.A. Zaghete, MRS Online Proce. Lib. Arch **1507**, 1–6 (2013)
26. B. Moongraksathum, D.S. Lee, Y.W. Chen, J. Taiwan Inst. Chem. Eng. **68**, 455–460 (2016)
27. W. Zou, C. Ge, M. Lu, S. Wu, Y. Wang, J. Sun, Y. Pu, C. Tang, F. Gao, L. Dong, RSC Adv. **5**, 98335–98343 (2015)
28. Q. Xu, D. Ju, Z. Zhang, S. Yuan, J. Zhang, H. Xu, B. Cao, Sens. Actuators B Chem. **225**, 16–23 (2016)
29. H. Xu, D. Ju, W. Li, J. Zhang, J. Wang, B. Cao, Sens. Actuators B. Chem. **228**, 634–642 (2016)
30. Q. Xu, Z. Zhang, X. Song, S. Yuan, Z. Qiu, H. Xu, B. Cao, Sens. Actuators B Chem. **245**, 375–385 (2017)
31. B. Liu, X. Zhao, C. Terashima, A. Fujishima, K. Nakata, Phys. Chem. Chem. Phys. **16**, 8751–8760 (2014)
32. F.-Q. Ma, J.-W. Yao, Y.-F. Zhang, Y. Wei, RSC Adv. **7**, 36288–36296 (2017)
33. L. Zhang, X. Yuan, H. Wang, X. Chen, Z. Wu, Y. Liu, S. Gu, Q. Jiang, G. Zeng, RSC Adv. **5**, 98184–98193 (2015)
34. T. Xian, H. Yang, J.F. Dai, Z.Q. Wei, J.Y. Ma, W.J. Feng, Mater. Lett. **65**, 3254–3257 (2011)
35. T. Puangpetch, S. Chavadej, T. Sreethawong, Energy Convers. Manag. **52**, 2256–2261 (2011)
36. T. Puangpetch, T. Sreethawong, S. Yoshikawa, S. Chavadej, J. Mol. Catal. A Chem. **312**, 97–106 (2009)
37. C. Jacoboni, *Theory of Electron Transport in Semiconductors: A Pathway from Elementary Physics to Nonequilibrium Green Functions*, 1st edn. (Springer, Berlin, 2010), p. 590
38. V. Diesen, M. Jonsson, J. Phys. Chem. C **118**, 10083–10087 (2014)
39. H. Jia, W. He, W.G. Wamer, X. Han, B. Zhang, S. Zhang, Z. Zheng, Y. Xiang, J.J. Yin, J. Phys. Chem. C **118**, 21447–21456 (2014)
40. S. Wu, J. Xiong, J. Sun, Z.D. Hood, W. Zeng, Z. Yang, L. Gu, X. Zhang, S.Z. Yang, ACS Appl. Mater. Interfaces. **9**, 16620–16626 (2017)
41. R. Schaub, P. Thostrup, N. Lopez, E. Lægsgaard, I. Stensgaard, J.K. Nørskov, F. Besenbacher, Phys. Rev. Lett. **87**, 266104 (2001)
42. V.M. Longo, A.T. De Figueiredo, S. De Lázaro, M.F. Gurgel, M.G.S. Costa, C.O. Paiva-Santos, J.A. Varela, E. Longo, V.R. Mastelaro, F.S. De Vicente, A.C. Hernandes, R.W.A. Franco, J. Appl. Phys. **104**, 23515 (2008)
43. S. Zhang, D. Guo, M. Wang, M.S. Javed, C. Hu, Appl. Surf. Sci. **335**, 115–120 (2015)